Nature Communications

https://doi.org/10.1038/s41467-026-73130-z

Article in Press

Spring–Summer Caribbean Sea marine heatwaves tied to previous Winter Indian Ocean marine heatwaves

Received: 13 June 2025

Accepted: 2 May 2026

Cite this article as: Li, Z., Li, J. Spring–Summer Caribbean Sea marine heatwaves tied to previous Winter Indian Ocean marine heatwaves. *Nat Commun* (2026). https://doi.org/10.1038/s41467-026-73130-z

Zeyu Li & Jianping Li

Spring–Summer Caribbean Sea Marine Heatwaves Tied to Previous Winter Indian Ocean Marine Heatwaves

Zeyu Li[1,2,3,4,5] and Jianping Li[*1,2,3,4,5,6]

[1] Frontiers Science Center for Deep Ocean Multi-spheres and Earth System (DOMES), Ocean University of China, Qingdao 266100, China

[2] Key Laboratory of Physical Oceanography, Ocean University of China, Qingdao 266100, China

[3] Academy of Future Ocean, Ocean University of China, Qingdao 266100, China

[4] College of Oceanic and Atmospheric Sciences, Ocean University of China, Qingdao 266100, China

[5] Center for Ocean Carbon Neutrality, Ocean University of China, Qingdao 266100, China

[6] Laboratory for Ocean Dynamics and Climate, Qingdao Marine Science and Technology Center, Qingdao 266237, China

***Corresponding author:**

Jianping Li (Email: ljp@ouc.edu.cn).

Abstract

Marine heatwaves can interact across ocean basins through atmospheric teleconnections, but such inter-basin links remain poorly understood. Here we show that boreal spring and summer marine heatwaves in the Caribbean Sea are significantly connected to marine heatwaves in the Indian Ocean during the preceding winter. Using observational data and climate model simulations, we identify that boreal winter Indian Ocean marine heatwaves trigger atmospheric convection, generating an eastward-propagating Indo-Pacific-Atlantic Rossby wave train. This wave train alters the regional Hadley circulation and renders the overlying atmosphere warm, moist, and stable over the Caribbean Sea, reducing latent heat loss from the ocean, driving sea surface warming and promoting the intensification of marine heatwaves. These findings reveal a robust teleconnection pathway that allows climate signals from one basin to amplify marine heatwaves in another.

Introduction

Marine heatwaves (MHWs) are extreme events of anomalous seawater warming. These events occur sporadically and can persist from days to months [1,2]. Numerous studies have investigated MHWs across diverse marine regions. Certain exceptionally intense MHWs have garnered significant interest, and have undergone comprehensive investigation on their origins, development, and impact assessment [3-7]. Oliver, et al. [8] provided a historical overview indicating that global MHWs have demonstrated a marked acceleration in warming trends, with an increase in both intensity and duration over time. Given the context of global warming, this trend is expected to continue, potentially resulting in an increased occurrence and severity of future MHWs [9,10].

MHWs imperil marine ecosystems by causing significant damage to biological resources, altering ecosystem structure, and negatively impacting industries such as aquaculture and marine tourism, leading to economic losses [11-16]. Moreover, MHWs in synergy with other extreme events like hurricanes or ocean acidification can amplify the severity of catastrophic outcomes [17-19]. To address and mitigate the impacts of MHWs, an urgent need exists for a thorough understanding of

MHWs. Recent studies have significantly advanced our knowledge of the origins and evolution of MHWs. Generally, MHWs can be triggered by anomalous air-sea heat fluxes due to atmospheric motion or by anomalous oceanic heat advection caused by anomalous currents [3,20,21]. These drivers may originate directly from the affected region[21-23] or be indirectly influenced by distant factors through complex oceanic and atmospheric processes[4,24,25]. In certain regions, well-researched factors contributing to MHWs include climate modes, oceanic or atmospheric planetary wave processes, and circulation changes due to high-pressure blocking etc. [24,26-29]. Historical data reveal that MHWs in specific regions exhibit distinct variability patterns, which some studies link to internal climate variability, regulated by background circulation and sea surface temperature (SST) changes [26,27,30-32]. This information aids in predicting MHW variability. Based on research into MHW drivers, some studies have successfully predicted MHWs using oceanic and atmospheric indices associated with MHWs or numerical models [33,34]. These indices can also be derived from MHWs themselves. Teleconnections linking MHWs to remote atmospheric and oceanic phenomena have been documented in earlier studies[35-38]. While teleconnection relationships among some extreme events have been identified through atmospheric Rossby waves [39], the exploration of such relationships in MHWs is still in its early stages. There may be underlying commonalities and interactions among MHWs in various areas, similar to other weather and climate systems. As a forcing at the atmospheric bottom boundary, MHWs can influence atmospheric motion, propagate their signals, and thereby affect MHWs in other regions, leading to teleconnections among them.

In the North Atlantic Ocean, the Caribbean Sea (CS) region (50° – 85°W, 8° – 24°N) experiences MHWs of lower intensity compared to those in western boundary current regions. Nonetheless, the destructiveness of these events in the CS is highly significant and warrants attention. Home to a vast number of coral reefs and a high level of biodiversity, CS is acutely sensitive to MHWs, contributing to their remarkable impact [11,40]. Additionally, many developing countries are located in the CS region, where traditional marine-related industries such as fishing are crucial to the local economy [41]. Despite the extensive research on high-intensity MHW regions, the study of MHWs in the CS remains an area for further investigation. The CS's unique geographical position, at the intersection of the northern hemisphere westerly belt and the tropical Hadley circulation, makes it particularly susceptible to the transmission of atmospheric waves from other regions via the

westerly waveguide. These atmospheric waves can influence upper-layer atmospheric dynamics, which in turn may affect MHWs in CS.

MHWs in the Indian Ocean (IO) have garnered increasing attention due to their profound impacts on regional climate, ecosystems, and fisheries[27,36]. These extreme warming events are often driven by a combination of large-scale climatic forcings and local air-sea interactions. Positive phases of the Indian Ocean Dipole (IOD) and El Niño–Southern Oscillation (ENSO) are recognized as key precursors, favoring basin-scale warming patterns that can intensify into MHWs in Indian Ocean[3,27,32]. Meanwhile, local oceanic processes—such as ocean heat advection and mixed-layer dynamics—also play crucial roles in their onset and persistence[31,42]. Separately, studies have shown that Indian Ocean variability can influence Atlantic climate via atmospheric teleconnections[43,44]. This raises a key question: can discrete, intense IO MHWs also trigger remote impacts on the Atlantic? The specific role of intense, localized MHW in forcing remote Atlantic extremes remains unclear.

In this work, we establish an inter-basin teleconnection between MHWs in the IO and those in the CS by analyzing observational data and climate model simulations. We propose an atmospheric bridge mechanism, in which boreal winter IO MHWs force an eastward-propagating Indo-Pacific-Atlantic Rossby wave train, which we partially reproduce in climate model simulations. This wave train induces anomalous regional Hadley circulation and reduces latent heat loss from the ocean, thereby driving sea surface warming and promoting the intensification of CS MHWs; local air–sea boundary layer conditions allow this anomalous warming to persist into the following spring and summer.

Results

Relationships between boreal winter Indian Ocean Marien heatwaves (MHWs) and the following spring (MAM) and summer (JJA) Caribbean Sea MHWs

Observational data indicate that IO MHWs during the DJF are often accompanied by subsequent MHWs in CS during the following spring (MAM) and summer (JJA) seasons (see Fig. S1&S2). To assess MHW events in these two regions, we develop marine heatwave index (MHWI) based on the regionally averaged monthly MHW days (50°–70°E, 0°–10°S for IO and 50°–85°W, 8°–

24°N for CS). The distribution of lead-lag correlation between the IO MHWI and CS MHWI (Fig. 1a) indicates that IO MHW generally leads CS MHWI across various months, with the lead-lag relationship being most pronounced in boreal winter (DJF). The lead time is approximately 3–6 months, suggesting that IO MHW in the DJF may be linked to CS MHW in the following spring (MAM) and summer (JJA). Subsequently, cross-spectral analysis was performed on the seasonally averaged IO MHWI from the previous boreal winter and the seasonally averaged CS MHW from the following spring (Fig. 1b) and summer (Fig. 1c). The results show significant coherence greater than 0.5 in the high-frequency portion, with nearly no phase lag. Fig. 1d shows the composite analysis of IO MHWI and CS MHWI before and after strong IO MHW events (shown in Tab. S1and Fig. S1). CS MHWI begins to increase after IO MHWI peaks in boreal winter, reaching its peak during the spring and summer seasons. We computed the lead-lag correlation between the DJF IO MHWI and the CS MHWI (Fig. 1e) and the results reveal a significant relationship between MHWs in IO during previous DJF and subsequent MHWs in the CS during April to July, occurring 3–6 months later (averaged $r = 0.56$, $p < 0.05$). Moreover, the MHW-based correlation is notably stronger and exhibits a sharper peak than that based on raw SST anomalies (Fig. S3). Notably, the two regions exhibit contrasting MHW seasonality and air–sea coupling characteristics: IO MHWs tend to influence the overlying atmosphere, whereas CS MHWs tend to be influenced by the atmosphere (Fig. S4). Based on the analysis of MHWs in the two sea areas, we speculate that the activity of DJF IO MHW can influence the concurrent and subsequent CS MHW through physical mechanisms.

The generation and propagation characteristics of the atmospheric bridge in Indo-Pacific-Atlantic Rossby wave tran.

Given that IO and the CS reside in different ocean basins, MHWs in the IO cannot directly influence the distant CS. The observed teleconnection, consequently, cannot be ascribed to direct oceanic processes. Instead, large scale atmospheric activities are typically linked to such cross-ocean-basin interactions [10]. We term this the Indo-Pacific-Atlantic teleconnection, which may potentially a eastward-propagating Rossby wave train (IPAT). We hypothesize that the signals and

energy from DJF IO MHWs are transmitted eastward to the North Atlantic Ocean via the IPAT, subsequently enhancing MHW activities in CS through local air-sea interactions.

During intense DJF IO MHWs, SST anomalies (SSTa) exceeding 0.5 °C were observed in the tropical western IO, particularly near and south of the equator (see Fig. S2a). Concurrently, the spatial pattern of MHW days anomalies closely resembled the distribution of SST anomalies. As depicted in Fig. S2a, compared to the climatological state, the MHW days in most regions of the tropical western IO increased by over 10 days per month during intense DJF IO MHWs. Anomalous SST warming in the equatorial Indian Ocean during intense DJF IO MHWs forms an atmospheric bridge that alters the overlying atmospheric circulation. Observations reveal that during intense DJF IO MHWs, ascending motions permeate the entire atmosphere over certain regions of the IO, with a center situated near the equator, corresponding to the active MHW center (Fig. S5a). Meanwhile, during strong DJF IO MHWs, significant precipitation anomalies occur over the equatorial western Indian Ocean and East Africa (Fig. S5b&c). These anomalies are likely associated with the warm SSTs of the IO MHWs, and similar conclusions regarding enhanced East African rainfall by warm Indian Ocean SSTs have been reported in previous studies[45,46]. The precipitation anomalies over the equatorial western Indian Ocean and East Africa may act as a disturbance to the upper-level atmosphere, thereby exciting Rossby wave activity. This indicates that the DJF IO MHWs can function as a perturbation, triggering upper atmospheric Rossby wave trains by influencing atmospheric ascending motions, thereby initiating the IPAT atmospheric bridge process. To ascertain the dynamic feasibility of the IPAT occurrence, we conducted an analysis of concurrent Rossby wave activity over the IO. Variations in the intensity of Rossby wave train activity were quantified by calculating changes in the Rossby wave source (RWS) at 200 hPa. Fig. S6 reveals a significant enhancement of the RWS near the active region of the DJF IO MHWs, indicating that the DJF IO MHWs can lead to increased concurrent Rossby wave activity over tropical western IO and East Africa. Additionally, stationary Rossby wave trajectories in 200 hPa isobaric surface were computed based on non-uniform horizontal basic flows for Rossby standing waves with zonal wave numbers ranging from 1 to 7 (Fig. 2a), focusing on the wave source above the tropical IO (0° – 10°S, 30° – 70°E). Then, based on the results of wave ray tracing, we calculated the Rossby wave ray flux (WRF) to better analyze the propagation paths and intensity (Fig. 2b). The results of the wave ray tracing and WRF depict the full trajectory of the Rossby wave train: generated over the equatorial Indian Ocean during intense DJF IO MHWs,

it initially propagates westward toward East Africa under the background easterlies. Subsequently, consistent with theoretical works[47-49] which posits that a southerly flow enables northward energy propagation, the wave train turns northward from East Africa to northern Africa and the Middle East. This path, steered by the background meridional flow, ultimately allows the tropical-originated wave train to reach the westerly wind belt, which guides it eastward to the North Atlantic. Fig. 2b depicts the anomalies of (30° – 70°E) meridional wind fields at the 200 hPa level during the intense DJF IO MHWs. Through the analysis of concurrent atmospheric circulation anomalies and WRF, several key atmospheric activity centers associated with IPAT can be identified, thereby elucidating its propagation path in the atmosphere. The trajectory of the wave rays in Fig. 2b aligns with the centers of atmospheric circulation anomalies, thereby affirming the dynamical rationality of the IPAT. Furthermore, a simulation experiment was conducted to investigate the remote correlation between the DJF IO MHWs and the IPAT, utilizing the CAM6 numerical model in aquaplanet mode. As illustrated in Fig. 2c, broadly reproduced the large-scale wave activity characteristics associated with the IPAT. Wave rays originating over the IO propagated westward till entering westerlies and then propagated eastward, exhibiting a trajectory consistent with observational data. Atmospheric wave activity centers also emerged in the low to middle latitudes of the Pacific and Atlantic Oceans, with the simulation producing local atmospheric circulation anomalies over the North Atlantic, though the detailed spatial pattern and amplitude differ from those in the reanalysis data. These discrepancies may be attributed to limitations in the aquaplanet setup, where the background wave guide is more zonal, leading to a more zonally oriented wave train. However, a similar meridional pattern happens over the CS, which in turn acts to reduce the Hadley cell circulation. Overall, the model simulation broadly reproduces the eastward propagation characteristics of the atmospheric wave train driven by DJF IO MHWs, exhibiting features analogous to those of the IPAT. We also used the data from ERA5 to support the conclusions presented in Fig. S5a and Fig. 2b (see Fig. S7).

The air-sea interaction of Indo-Pacific-Atlantic Rossby wave train in the Caribbean Sea and its impact on spring (MAM) and summer (JJA) Caribbean Sea MHWs.

During DJF, IPAT transmits signals from the IO to the Pacific and North Atlantic via Rossby wave trains. To elucidate the atmospheric response over the North Atlantic to this signal during the concurrent period, we investigated the convergence and divergence in the upper atmosphere at 200 hPa, as well as the vertical motion in the middle atmosphere at 500 hPa (Fig. 3a). Significant convergence and divergence movements in the upper atmosphere, resulting from Rossby wave activity, are observed during the intense DJF IO MHWs, thereby inducing ascending and descending motions in the middle atmosphere. The activity centers of atmospheric sinking and rising are respectively located near the equator to the south of the CS (10°S – 10°N) and in the mid-to-low latitude regions to the north (20° – 30°N). To investigate the impact of these movement patterns dipole in the meridional direction on the ocean, we examined the dynamical and thermal characteristics of the entire atmospheric column during intense DJF IO MHWs, thereby analyzing the influence of the DJF IPAT signals on the concurrent North Atlantic atmosphere from both dynamical and thermal perspectives. From a dynamical perspective, the DJF atmospheric convergence and divergence result in downward motion near the equator and upward motion in the middle and low latitudes, favoring the formation of a concurrent anti-Hadley circulation anomaly that is opposite to the background circulation (Fig. S8). Consequently, this anomaly in DJF attenuates the vertical motion of the atmosphere and generates an anomalous southerly wind over the CS concurrently. From a thermal perspective, the entire atmospheric column over the North Atlantic has undergone warming of varying magnitudes during intense DJF IO MHWs. This phenomenon is attributed to atmospheric adjustments in response to wave activity, leading to an increase in the geopotential height of the entire atmospheric layer, which in turn results in an enhancement of atmospheric thickness (see Fig. S9a). Li, et al. [50] demonstrate that an increase in atmospheric thickness contributes to the warming of the entire atmospheric layer. Notably, the amplitude of warming in the higher atmospheric levels exceeds that in the lower levels, typically suggesting a more stable atmospheric structure and diminished convection.

The influence of large-scale atmospheric activities on SST primarily mediated through heat flux at the air-sea interface [51-53]. To verify the role of air-sea interface heat flux in the warm SSTa in the Caribbean Sea, a mixed-layer heat budget analysis within CS region during and after the intense DJF IO MHW period is performed, and the results indicate that anomalous reduction in latent heat loss is the primary driver of the mixed-layer SST anomalies in the CS following IO MHWs, accounting for 82% of the variance. (Fig. S10). Consistent with the methodological framework of

Gupta, et al. [32], we further examine the daily SST during the 3–6 months following DJF IO MHW events and found that mean SST is significantly higher than climatology ($p < 0.01$) while the variance shows no significant difference ($p = 0.06$; Fig. S11). This indicates that the increased CS MHW activity is primarily driven by the rise in background SST—a direct consequence of the atmospheric forcing identified above—rather than by changes in daily variability. This atmospheric forcing is manifested in the large-scale circulation anomalies shown in Fig. 3c, where the meridional atmospheric movement dipole has induced a dipole of circulation anomalies in the lower atmosphere. Regions of abnormal atmospheric descent (ascent) at 500 hPa transform into concurrent anomalous anticyclonic (cyclonic) centers in the lower atmosphere at 925 hPa. The anomalous anticyclone in the southern CS and the anomalous cyclone in the north form a flow field that is consistent with the anomalous southerly winds in the lower part of the abnormal Hadley circulation, both of which can explain the cause of the anomalous southerly winds at the sea surface. The anomalous southerly winds, being opposite in direction to the background wind field, weaken the local background wind field and consequently reduce the sea surface wind speed. Simultaneously, this also facilitates the influx of warmer and more humid air from equatorial regions in DJF, thereby decreasing the temperature and humidity differences at the air-sea interface (see Fig. S9b). The warming of the entire atmospheric layer, including an increase in sea surface air temperature, reduces the temperature difference at the air-sea interface. Under the influence of various factors, the evaporation of seawater in the CS is suppressed during intense DJF IO MHWs, leading to an anomalous reduction in the latent heat loss at the air-sea interface and the activate of DJF CS MHW. To assessing the impact of the DJF IO MHW on the CS MHW during subsequent spring (MAM) and summer (JJA) seasons, we computed the Hadley Cell Index (HCI), air-sea interface temperature difference (dT), relative humidity, and latent heat flux (positive when warming the ocean) at the air-sea interface for the CS regional average (50° – 85°W, 8° – 24°N) over a few months before and after the occurrence of the DJF IO MHW (Fig. 3d). The HCI is defined as the difference between the zonal wind speed component at 850 hPa and that at 200 hPa. During the intense DJF IO MHW, the anomalous Hadley circulation, the increase in low-level atmospheric humidity, and the decrease in dT all remain relatively significant for the subsequent two months and exhibit no drastic changes within 3 to 5 months following the DJF IO MHW, but instead stabilize near the climatological norm. In other words, the signals triggered by the DJF IO MHW can enhance the activity of the CS MHW during the same period and the subsequent two

months, which corresponds to the gradual activation of concurrent CS MHW. And this circulation environment does not decay over the next 3 to 5 months, instead remaining in an active state, which facilitates the activity of CS MHWs to remain strong during spring (MAM) and summer (JJA). This phenomenon warrants further investigation, as anomalous warm sea surface temperatures (SST) typically elicit surface heat flux feedback that damps the warm SST anomalies, preventing their prolonged persistence [51,54,55].

The Marine Atmospheric Boundary Layer (MABL) plays a significant role in the thermodynamic adjustment of SSTa in the surface heat flux feedback [56-58]. The MABL is a layer of the lower atmosphere close to the sea surface. In this layer, the physical properties of the air are relatively uniform in the vertical direction, and vertical motion is intense. Due to the limited heat content and moisture-holding capacity of the air within the MABL, the atmosphere near the sea surface rapidly reaches thermal equilibrium with the seawater after absorbing heat and water vapor from it, and no further heat exchange takes place between them [54]. At this point, the intense vertical motion within the MABL can eliminate the temperature and humidity anomalies in the lower air through mixing and transport, disrupting the thermal equilibrium at the air-sea interface and allowing the seawater to continue to lose heat to the air. This process is influenced by the stability and thickness of the MABL, as well as the physical characteristics of the air over the sea surface [59-63].

However, as discussed previously, the differential warming of atmosphere induced by the DJF IPAT signal exerts a significant influence on the concurrent MABL characteristics. The warming in the upper layer caused by the IPAT is more intense than that in the lower layer (Fig. 3b), which facilitates an increase in the stability of the MABL. Additionally, the anomalous anti-Hadley cell in DJF has caused an enhancement of wind shear and a thinner MABL in the lower atmosphere over CS region (Fig. S9c). These factors result in a more stable MABL, which suppresses the upward vertical movement of air during intense DJF IO MHWs [59,61,63,64]. The ability of the air at the sea surface to remove the warm and moist imprint from the underlying seawater through vertical mixing is weakened, impeding the process of heat loss from the sea to the atmosphere. The abnormal water vapor on the surface of the CS persists from the previous winter (DJF) to summer (JJA), corroborating this process (Fig. 3d). This process ultimately manifests as the latent heat flux not showing a significant anomaly during spring (MAM) and summer (JJA) as expected in the surface heat flux feedback process to cool the sea surface temperature, preventing the MHW

activity from returning to the climatological norm. Instead, it merely maintains the latent heat flux near the climatological norm, prolonging the impact of the IPAT signal on the CS MHW and keeping it active from previous winter to summer (JJA). We also used the data from ERA5 to support the conclusions presented in Fig. 3a and Fig. 3b (see Fig. S7).

Discussion

This study identifies a potential seasonal teleconnection between MHWs in the previous winter IO basin and those in the spring (MAM) and summer (JJA) Atlantic Ocean basins, elucidating the role of atmospheric processes in this phenomenon. In this study, we calculated the MHW indices of the equatorial western IO and the CS using OISST observation data. Through lead-lag correlation analysis, a significant correlation was found between the DJF IO MHW and the CS MHW, with the DJF IO MHW leading the CS MHW by 3 to 6 months. To explain this cross-ocean basin seasonally scaled MHW teleconnection, this study proposed an atmospheric bridge process based on the eastward-propagating atmospheric Rossby wave trains: The previous boreal winter IO MHWs perturb the upper atmosphere and enhance precipitation above the West Indian Ocean and the East Africa, with the generated signals transmitted to the North Atlantic concurrently via Rossby wave trains. This triggers local air-sea interactions, thereby enhancing the DJF CS MHWs and sustaining into the summer (JJA) season. We performed a composite analysis of the DJF IO MHW using oceanic and atmospheric observations and utilized the CAM6 model to simulate and validate several of the proposed physical processes. A case study of the 1986–1987 DJF IO MHW confirms the robustness of the composite results (Fig. S12 – S16). The proposed physical mechanism, detailed in Fig. 4, illustrates how CS MHWs tied to DJF IO MHWs. During previous winter, the MHW-induced heating of the atmosphere over the IO generates upward motion, perturbing the upper atmosphere, causing the geopotential height over the equatorial IO to rise; the Rossby wave activity in the upper atmosphere of the equatorial IO is enhanced, and the wave train transmits the signal concurrently to the upper layer above CS along the westerlies in the Indo-Pacific-Atlantic Rossby wave train (IPAT) teleconnection pattern, forming an atmospheric bridge connecting the two regions during the intense DJF IO MHWs (Fig. 4a); Fig. 4b describes the concurrent local air-sea interaction process in CS. The Rossby waves coming through the atmospheric bridge form atmospheric convergence and divergence over the North Atlantic, and

the resulting upward and downward atmospheric motions constitute an anomalous anti-Hadley circulation, while increasing the thickness of atmosphere causes warming. Subsequently, this anti-Hadley circulation has multiple effects: the southerly anomaly in the lower atmosphere weakens the background wind field, suppresses vertical motion of the atmosphere, and promotes the advection of warm and humid air over the CS; it also suppresses the vertical motion of the atmosphere and reduces the vertical mixing. For the ocean in DJF, a decrease in sea surface wind speed and the increase in air temperature and humidity inhibit seawater evaporation, leading to a deficit of latent heat cooling compared to climatology, favoring the activation of DJF CS MHWs. Subsequently, these conditions favor an equilibrium between atmospheric boundary layer and marine mixed layer, hindering ocean cooling by evaporation , promoting the persistence of CS MHWs' activity into spring (MAM) and summer (JJA) (Fig. 4c).

The potential modulating role of the IOD and the ENSO in the IO–CS MHW teleconnection warrants careful discussion. Both IOD and ENSO are known to strongly influence the variability of MHWs in the Indian Ocean[27,37], and they also exert remote effects on Atlantic SST[65-67]. It is therefore plausible that they contribute to establishing the large-scale background state that facilitates the IO–CS MHW teleconnection. However, in this study, several lines of evidence suggest that the identified lagged relationship remains, to a certain extent, independent of these dominant climate modes. Statistically, after removing the signals of IOD and ENSO from the MHW indices through filtering, a significant association persists between the IO and CS MHWI, retaining 51% of the original variance (Fig. S17 and Tab. S2). In contrast, the original ENSO–CS MHW correlation (ENSO leads CS MHWI by 5 months) is 0.44 (R^2 = 19.4%). After removing the influence of IO MHWs from CS MWHI, the partial correlation drops to 0.19 (R^2 = 3.6%, $p < 0.05$), retaining only 18% of the original ENSO–CS MHW variance (Tab. S2 and Fig. S18). The original IOD–CS MHW correlation is 0.35 (R^2 = 12.3%); after controlling for IO MHWI, it falls to 0.07 (R^2 = 0.5%, p = 0.41), retaining only 4% of the original variance (Tab. S2 and Fig. S19). These results2 demonstrate that the apparent relationships of ENSO and IOD with CS MHWs are largely mediated through the Indian Ocean, while the IO–CS MHW teleconnection retains a substantial component independent of these climate modes. Dynamically, the atmospheric response pattern—characterized by a mid-latitude Rossby wave train extending from the Indian Ocean to the Caribbean Sea—differs from the typical east–west overturning circulations usually perturbed by ENSO or IOD. This is supported by the absence of robust, basin-wide zonal wind anomalies in the

tropical Atlantic lower troposphere during IO MHW events (Fig. S20), which would be expected if the teleconnection were primarily mediated by an altered Walker circulation. Furthermore, after removing the ENSO and IOD signals, the anomalous anti-Hadley circulation over the Caribbean Sea during IO MHW shows no fundamental change (Fig. S21). In summary, although IOD and ENSO may shape the background conditions and could potentially enhance the connection between IO MHWs and CS MHWs, the specific 3–6 month lagged linkage with CS MHWs appears to be primarily channeled through the IPAT mechanism. This study highlights that extreme regional SST warming event in the Indian Ocean, even when partially embedded within larger-scale climate variability, may activate distinct atmospheric pathways that subsequently influence marine heatwaves in the remote Caribbean Sea.

This study identifies a distinct pathway for inter-basin teleconnection that differs from the canonical mechanisms emphasized in prior literature. Previous investigations into ocean-atmosphere linkages involving the Pacific have largely highlighted the central role of large-scale adjustments in the equatorial Walker Circulation[68,69]. Furthermore, as noted by Wang [65], the specific processes by which the Indian Ocean actively influences North Atlantic climate remain insufficiently understood, with existing research focusing primarily on equatorial Atlantic variability or basin-scale modes. Against this backdrop, our findings reveal a distinct mid-latitude Rossby wave train mechanism. The IPAT originates from SST forcing associated with IO MHW and propagates eastward via the Northern Hemisphere mid-latitude westerly waveguide, directly impacting the subtropical Caribbean Sea—a key extratropical region of the North Atlantic not previously identified as a primary target of such a teleconnection. Unlike the zonally oriented Walker Cell adjustments, this pathway operates through meridional modulation of the local Hadley circulation over the Caribbean Sea, thereby affecting low-level winds and surface heat fluxes. Thus, our work not only addresses the mechanistic gap highlighted in earlier studies but also delineates a previously overlooked extratropical route of Indian Ocean influence, offering a refined perspective on how regional extreme warming can remotely orchestrate climate extremes in another ocean basin.

Existing studies have pointed out that numerous oceanic and atmospheric processes have important impacts on MHW [4,24,27,70,71]. Based on these studies, many predictive analysis methods for MHW have been proposed [4,33,34]. However, these studies lack the research on the interaction between MHWs themselves, which is the focus of this study. By analyzing the interaction between MHW

and the atmosphere and combining the connecting role of the atmospheric bridge, this study extends the connection to that between one MHW and another, proving that MHWs can also interact with each other and form teleconnections like other weather and climate systems, enabling us to understand MHW from a broader perspective. The observed lead-lag relationship between MHWs may be a common feature in other oceanic regions, offering a potential seasonal-scale predictor for MHW occurrences and holding significant potential for enhancing the prevention and mitigation strategies against MHW-related disasters.

Methods

Observations

In this study, the sea surface temperature (SST) data employed for the investigation of marine heatwaves is sourced from the Daily Optimum Interpolation Sea Surface Temperature version 2.1 (OISSTv2.1) provided by the National Oceanic and Atmospheric Administration [72]. This dataset has a spatial resolution of a 0.25°×0.25° grid and has been available since September 1st, 1981.

The atmospheric data, including omega (Vertical velocity ω in Pa s^{-1}, where $\omega = \mathrm{d}p/\mathrm{d}t$, negative values indicate upward motion.), temperature, low-level atmospheric humidity (average of 1000 and 925 hPa specific humidity) and winds, are obtained from the NCEP/NCAR reanalysis monthly mean dataset [73]. We utilized the portion of this dataset spanning from 1982 to 2024 on a 2.5°×2.5° grid with 17 pressure levels. Precipitation data is obtained from Global Precipitation Climatology Centre (GPCC)[74] monthly precipitation dataset with a spatial resolution of 1° × 1° and the monthly mean Climate Prediction Center Merged Analysis of Precipitation (CMAP)[75] dataset from 1982 to 2024. Additionally, the monthly net heat flux data (defined as positive when downward), 2-meter air temperature, sea surface temperature, and boundary layer height data are obtained from the ECMWF Reanalysis v5 (ERA5) dataset, which has a spatial resolution of 0.25°×0.25° [76]. The air–sea temperature difference is computed from the 2-meter air temperature and SST. These data are used to understand the heat transfer situation between the ocean and the atmosphere. To mitigate the contingency of the dataset, all conclusions drawn from the NCEP data were compared and verified with the ERA5 data. We used all data from 1982 to 2024, with the linear trend removed.

Anomalies were calculated by subtracting the climatology for the period 1981–2010 from the monthly mean data.

Definition of marine heatwaves

Marine heatwaves are identified following Hobday, et al. [1]. where a MHW is defined as a discrete prolonged anomalously warm water event during which daily sea surface temperature (SST) exceeds the seasonally varying 90th percentile threshold for at least five consecutive days. A fixed-baseline definition is adopted in this study. We explore the MHWs from 1982 to 2024 using the OISSTv2.1 dataset on each grid. The linear trend has been removed from the SST data to eliminate the influence of global warming on MHWs, and the entire available period (1982–2024) is used as the baseline. The number of MHW days is defined as the total duration during which MHW occurs within a specific time period (unit: days). To assess MHW events in a region, a marine heatwave index (MHWI) has been developed which is based on the regionally averaged monthly MHW days. The IO MHWI is defined as the average of the monthly MHW days within the range of 0° – 10°S and 50° – 70°E. The CS MHW Index is defined in a similar manner to the IO MHWI, but its region is specified as 8° – 24°N and 50° – 85°W. The annual cycles of MHW days and the seasonally averaged MHW thresholds for the two regions are shown in Fig. S22 and Fig. S23, respectively.

Given the extreme nature of MHW events, to better capture their characteristics, more attention should be paid to the periods when significantly intense MHWs occur. Thus, in this study, a composite analysis of several intense IO MHWs is carried out to reveal the impacts of MHWs on both the ocean and the atmosphere. After removing the linear trend and the annual cycle, events in which the IO MHWI in boreal winter (December, January and February, DJF for short) exceeds one standard deviation are defined as strong DJF IO MHWs. The specific time details can be found in the supporting document (see Tab. S1).

Rossby wave source and Rossby wave ray

To more accurately describe the atmospheric bridge between IO and CS from a dynamic perspective, the Rossby wave source (RWS) and wave ray tracing theory [48,77-79] were utilized in this study. The definition of RWS [80] is given by

$$RWS = -\nabla \cdot (\boldsymbol{v}_\chi \zeta) = -(\zeta \nabla \cdot \boldsymbol{v}_\chi + \boldsymbol{v}_\chi \cdot \nabla \zeta) \quad (1)$$

where $\boldsymbol{v}_\chi$ is the divergent component of the horizontal wind and ζ is the absolute vorticity.

For wave tracing, the stationary Rossby wave ray trajectories theory is developed by Hoskins and Karoly [81] and extended by Li et al.[48,49] to incorporate the meridional component of the background flow and enable cross-equatorial Rossby wave propagation. This framework assumes a horizontally nonuniform basic flow and defines the local group velocity $\boldsymbol{c}_g = (u_g,\ v_g)$ defined by as

$$u_g = \bar{u}_M + \frac{\left[\frac{(k^2 - l^2)\,\partial \bar{q}}{\partial y} - \frac{2kl\,\partial \bar{q}}{\partial x}\right]}{K^4} \quad (2a)$$

$$v_g = \bar{v}_M + \frac{\left[\frac{2kl\,\partial \bar{q}}{\partial y} + \frac{(k^2 - l^2)\,\partial \bar{q}}{\partial x}\right]}{K^4} \quad (2b)$$

where $(\bar{u}_M, \bar{v}_M) = [\bar{u}(\lambda, \varphi), \bar{v}(\lambda, \varphi)] / \cos \varphi$ is the Mercator projection of the basic states of zonal and meridional winds, λ and φ represent the longitude and latitude, respectively, k and l are the zonal and meridional wavenumbers, respectively, $K = \sqrt{k^2 + l^2}$ is the total wavenumber, and $\bar{q} = 2\sin \varphi + \nabla 2\bar{\psi}$ is the basic-state absolute vorticity. Variable $\bar{\psi}$ is the basic-state stream function. Then there are

$$\frac{\mathrm{D}_g k}{\mathrm{D}t} = -k\frac{\partial \bar{u}_M}{\partial x} - l\frac{\partial \bar{v}_M}{\partial x} + \frac{\frac{k\partial^2 \bar{q}}{\partial y\,\partial x} - \frac{l\,\partial^2 \bar{q}}{\partial x^2}}{K^2} \quad (3a)$$

$$\frac{\mathrm{D}_g l}{\mathrm{D}t} = -k\frac{\partial \bar{u}_M}{\partial y} - l\frac{\partial \bar{v}_M}{\partial y} + \frac{\frac{k\partial^2 \bar{q}}{\partial y^2} - \frac{l\partial^2 \bar{q}}{\partial x\,\partial y}}{K^2} \quad (3b)$$

where $\frac{\mathrm{D}_g}{\mathrm{D}t} = \frac{\partial}{\partial t} + c_{\boldsymbol{g}} \cdot \nabla_M$ is the material derivative moving with the wave ray. Numerical integration using Eqs. (2) and (3) shows the stationary Rossby wave ray trace ($\omega = 0$) in a horizontally nonuniform basic flow.

This study employs the horizontal Rossby wave ray flux (WRF) method proposed by Yang and Li[82]. This method integrates both Lagrangian trajectory information and Eulerian local flux characteristics, making it applicable to tropical regions and capable of distinguishing the influence

of different wave sources. The WRF is defined as the flow of wave rays passing through a unit grid area per unit time:

$$\boldsymbol{F}_{WR} = \frac{1}{S_\varphi} \iint_{S_\varphi} \boldsymbol{V}_R \mathrm{d}S_\varphi \tag{4}$$

where $\boldsymbol{F}_{WR}$ is the average propagation velocity of the wave ray, and S_φ is the grid area. The wave ray velocity is calculated as:

$$\bar{u}_R = a\cos\varphi \frac{\Delta\lambda_R}{\Delta t}, \qquad \bar{v}_R = a\frac{\Delta\varphi_R}{\Delta t} \tag{5}$$

Here, a is the Earth's radius, φ is the latitude, $\Delta\lambda_R$ and $\Delta\varphi_R$ are the longitudinal and latitudinal distances traveled by the ray through the grid, and Δt is the transit time.

Numerical simulation

To investigate the influences of the preceding DJF IO MHW, numerical simulations were performed with the Community Atmosphere Model Version 6 (CAM6). The QPC6 component set is selected for CAM6, which employed the assumption of aquaplanet and driven by a prescribed SST field. The simulations use a 1.9° (lat) ×2.5° (lon) horizontal grid resolution, with a 32-hybrid sigma-pressure levels.

We design two CAM6 experiments using different lower boundary conditions: one climatology control and one forcing simulation that are designed to investigate sensitivity to strong DJF IO MHW forcing. For the forcing experiment, we linearly superimpose the average SST anomaly during the strong DJF IO MHW period onto the climatology in the equatorial IO, and we apply smoothing to the boundaries to eliminate abrupt SST gradients. The simulations are performed for 30 years, and the last 20 years of each is used for our analysis.

Cross-Spectral Analysis

To investigate the frequency-dependent relationship between IO MHWI and CS MHWI time series, we employed the Blackman-Tukey method of cross-spectral analysis[83]. For the two discrete time series, $x(t)$ and $y(t)$ (where $t = 1,2,\ldots,n$), the auto-spectra ($P_{xx}(f)$ and $P_{yy}(f)$) and the cross-spectrum ($P_{xy}(f)$) were estimated. This was achieved by first computing the auto-covariance

and cross-covariance functions up to a maximum lag m, where m was chosen to be approximately $n/5$ to balance spectral resolution against the stability of the estimates[84]. A lag window is then applied to these covariance functions before performing the Fourier transform to obtain the spectra [83,84]. From the resulting cross-spectrum, the squared coherency spectrum and lag spectrum are derived.

From the cross-spectrum, which is a complex number, we derived two key quantities. First, the squared coherency spectrum, defined as:

$$R_{xy}^2(f) = \frac{| P_{xy}(f) |^2}{P_{xx}(f)P_{yy}(f)} \tag{6}$$

measures the linear correlation between the two series at each frequency f, with values ranging from 0 to 1.

Second, the phase spectrum, $\phi_{xy}(f)$, was calculated from the cross-spectrum. It indicates the phase lead/lag relationship between the components of the two series at a given frequency. This phase information was then used to compute the lag spectrum, $L_{xy}(f)$, which converts the phase angle into a time delay:

$$L_{xy}(f) = \frac{\phi_{xy}(f) \cdot T(f)}{2\pi} \tag{7}$$

where $T(f) = 1/f$ is the period. A positive (negative) phase indicates that $y(t)$ leads (lags) $x(t)$.

The statistical significance of the coherence estimates was assessed using an F-test at the 95% confidence level. The test accounts for the degrees of freedom $\nu = (2n - m/2)/m$ inherent in the smoothed spectral estimates. The critical value for coherence is derived from the F-distribution with 2 and $2(\nu - 1)$ degrees of freedom.

Significance test

The statistical significance in the linear correlation analysis between two autocorrelated series is examined by the two-tailed Student's t-test with the effective number of degrees of freedom (Neff) given by:

$$\frac{1}{N_{eff}} \approx \frac{1}{N} + \frac{2}{N}\sum_{j=1}^{N}\frac{N-j}{N}\rho_{XX}(j)\rho_{YY}(j) \quad (8)$$

where N denotes the sample size and ρ_{XX} (j) stands for the autocorrelation of sampled time series X and ρ_{YY} (j) is for Y, while j is the time lag [85]. The data were assumed to follow a normal distribution.

Data Availability

The OISST data used in this study are available in the NOAA repository under https://psl.noaa.gov/data/gridded/data.noaa.oisst.v2.highres.html. The NCEP/NCAR Reanalysis data used in this study are available in the NOAA repository under https://psl.noaa.gov/data/gridded/data.ncep.reanalysis.html. The ERA5 data used in this study are available in the Copernicus Climate Data Store under https://cds.climate.copernicus.eu/. The GPCC precipitation data used in this study are available in the NOAA repository under https://psl.noaa.gov/data/gridded/data.gpcc.html. The CMAP precipitation data used in this study are available in the NOAA repository under https://psl.noaa.gov/data/gridded/data.cmap.html.

Code Availability

The analysis codes used in this study have been deposited in Zenodo under the following DOI: https://doi.org/10.5281/zenodo.19788288. The codes are written in MATLAB, utilizing the M_Map toolbox for map visualizations. All maps were generated using MATLAB 2023b.

References

1. Hobday, A. J. *et al.* A hierarchical approach to defining marine heatwaves. *PROGRESS IN OCEANOGRAPHY* **141**, 227-238, doi:10.1016/j.pocean.2015.12.014 (2016).

2. Pearce, A. F. & Feng, M. The rise and fall of the "marine heat wave" off Western Australia during the summer of 2010/2011. *JOURNAL OF MARINE SYSTEMS* **111**, 139-156, doi:10.1016/j.jmarsys.2012.10.009 (2013).

3. Holbrook, N. J. *et al.* A global assessment of marine heatwaves and their drivers. *NATURE COMMUNICATIONS* **10**, doi:10.1038/s41467-019-10206-z (2019).

4. Li, Z., Holbrook, N. J., Zhang, X., Oliver, E. C. J. & Cougnon, E. A. Remote Forcing of Tasman Sea Marine Heatwaves. *Journal of Climate* **33**, 5337-5354, doi:https://doi.org/10.1175/JCLI-D-19-0641.1 (2020).

5. Elzahaby, Y., Schaeffer, A., Roughan, M. & Delaux, S. Oceanic Circulation Drives the Deepest and Longest Marine Heatwaves in the East Australian Current System. *Geophysical Research Letters* **48**, e2021GL094785, doi:https://doi.org/10.1029/2021GL094785 (2021).

6. Di Lorenzo, E. & Mantua, N. Multi-year persistence of the 2014/15 North Pacific marine heatwave. *Nature Climate Change* **6**, 1042-1047, doi:10.1038/nclimate3082 (2016).

7. Amaya, D. J., Miller, A. J., Xie, S.-P. & Kosaka, Y. Physical drivers of the summer 2019 North Pacific marine heatwave. *Nature Communications* **11**, 1903, doi:10.1038/s41467-020-15820-w (2020).

8. Oliver, E. C. J. *et al.* Longer and more frequent marine heatwaves over the past century. *NATURE COMMUNICATIONS* **9**, doi:10.1038/s41467-018-03732-9 (2018).

9. Frölicher, T. L., Fischer, E. M. & Gruber, N. Marine heatwaves under global warming. *NATURE* **560**, 360-+, doi:10.1038/s41586-018-0383-9 (2018).

10. Holbrook, N. J. *et al.* Keeping pace with marine heatwaves. *NATURE REVIEWS EARTH & ENVIRONMENT* **1**, 482-493, doi:10.1038/s43017-020-0068-4 (2020).

11. Ilosvay, X. E. E., Contreras-Silva, A. I., Alvarez-Filip, L. & Wild, C. Coral Reef Recovery in the Mexican Caribbean after 2005 Mass Coral Mortality-Potential Drivers. *DIVERSITY-BASEL* **12**, doi:10.3390/d12090338 (2020).

12. Babcock, R. C. *et al.* Severe Continental-Scale Impacts of Climate Change Are Happening Now: Extreme Climate Events Impact Marine Habitat Forming Communities Along 45% of Australia's Coast. *Frontiers in Marine Science* **6**, doi:10.3389/fmars.2019.00411 (2019).

13. Zamoner, J. B. *et al.* Integrating Oceanographic Data and Benthic Community Structure Temporal Series to Assess the Dynamics of a Marginal Reef. *FRONTIERS IN MARINE SCIENCE* **8**, doi:10.3389/fmars.2021.762453 (2021).

14. Mills, K. E. *et al.* Fisheries Management in a Changing Climate Lessons from the 2012 Ocean Heat Wave in the Northwest Atlantic. *OCEANOGRAPHY* **26**, 191-195, doi:10.5670/oceanog.2013.27 (2013).

15. Eaton, K. M., Hallaj, A., Stoeckel, J. A. & Bernal, M. A. Ocean Warming Leads to Increases in Aerobic Demand and Changes to Gene Expression in the Pinfish (Lagodon rhomboides). *FRONTIERS IN ECOLOGY AND EVOLUTION* **9**, doi:10.3389/fevo.2021.809375 (2022).

16. Smith, K. E. *et al.* Socioeconomic impacts of marine heatwaves: Global issues and opportunities. *Science* **374**, eabj3593, doi:doi:10.1126/science.abj3593 (2021).

17. Burger, F. A., Terhaar, J. & Frölicher, T. L. Compound marine heatwaves and ocean acidity extremes. *Nature Communications* **13**, 4722, doi:10.1038/s41467-022-32120-7 (2022).

18. Dzwonkowski, B. *et al.* Compounding impact of severe weather events fuels marine heatwave in the coastal ocean. *Nature Communications* **11**, 4623, doi:10.1038/s41467-020-18339-2 (2020).

19. Choi, H.-Y., Park, M.-S., Kim, H.-S. & Lee, S. Marine heatwave events strengthen the intensity of tropical cyclones. *Communications Earth & Environment* **5**, 69, doi:10.1038/s43247-024-01239-4 (2024).

20. Oliver, E. C. J. *et al.* in *ANNUAL REVIEW OF MARINE SCIENCE, VOL 13, 2021* Vol. 13 (eds C. A. Carlson & S. J. Giovannoni) 313-342 (2021).

21. Bian, C., Jing, Z., Wang, H. & Wu, L. Scale-Dependent Drivers of Marine Heatwaves Globally. *Geophysical Research Letters* **51**, e2023GL107306, doi:https://doi.org/10.1029/2023GL107306 (2024).

22. Oliver, E. C. J. *et al.* The unprecedented 2015/16 Tasman Sea marine heatwave. *Nature Communications* **8**, 16101, doi:10.1038/ncomms16101 (2017).

23. Sugimoto, S., Qiu, B. & Kojima, A. Marked coastal warming off Tokai attributable to Kuroshio large meander. *Journal of Oceanography* **76**, 141-154, doi:10.1007/s10872-019-00531-8 (2020).

24. Song, Q., Wang, C., Yao, Y. & Fan, H. Unraveling the Indian monsoon's role in fueling the unprecedented 2022 Marine Heatwave in the Western North Pacific. *npj Climate and Atmospheric Science* **7**, 90, doi:10.1038/s41612-024-00645-x (2024).

25. Liu, H., Zhang, L., McPhaden, M. J., Han, W. & Li, H. Positive Indian Ocean Dipole intensifies marine heatwaves in the tropical southeast Atlantic coastal region. *Science Advances* **11**, eadx8525, doi:doi:10.1126/sciadv.adx8525 (2025).

26. Scannell, H. A., Pershing, A. J., Alexander, M. A., Thomas, A. C. & Mills, K. E. Frequency of marine heatwaves in the North Atlantic and North Pacific since 1950. *Geophysical Research Letters* **43**, 2069-2076, doi:https://doi.org/10.1002/2015GL067308 (2016).

27. Qi, R., Zhang, Y., Du, Y. & Feng, M. Characteristics and Drivers of Marine Heatwaves in the Western Equatorial Indian Ocean. *Journal of Geophysical Research: Oceans* **127**, e2022JC018732, doi:https://doi.org/10.1029/2022JC018732 (2022).

28. Chiswell, S. M. Atmospheric wavenumber-4 driven South Pacific marine heat waves and marine cool spells. *Nature Communications* **12**, 4779, doi:10.1038/s41467-021-25160-y (2021).

29. Yao, Y. & Wang, C. Variations in Summer Marine Heatwaves in the South China Sea. *Journal of Geophysical Research: Oceans* **126**, e2021JC017792, doi:https://doi.org/10.1029/2021JC017792 (2021).

30. Ren, X., Liu, W., Capotondi, A., Amaya, D. J. & Holbrook, N. J. The Pacific Decadal Oscillation modulated marine heatwaves in the Northeast Pacific during past decades. *Communications Earth & Environment* **4**, 218, doi:10.1038/s43247-023-00863-w (2023).

31. Das, D. & Mohanty, S. Progression of marine heat wave events over the tropical Indian Ocean and its underlying mechanisms. *Deep Sea Research Part II: Topical Studies in Oceanography* **219**, 105438, doi:https://doi.org/10.1016/j.dsr2.2024.105438 (2025).

32. Gupta, H., Deogharia, R., Sil, S. & Dey, D. Characteristics of Marine Heat Extreme Evolution in the Northern Indian Ocean. *International Journal of Climatology* **45**, e8734, doi:https://doi.org/10.1002/joc.8734 (2025).

33. Koul, V. *et al.* Seasonal Prediction of Arabian Sea Marine Heatwaves. *Geophysical Research Letters* **50**, e2023GL103975, doi:https://doi.org/10.1029/2023GL103975 (2023).

34. Jacox, M. G. *et al.* Global seasonal forecasts of marine heatwaves. *Nature* **604**, 486-490, doi:10.1038/s41586-022-04573-9 (2022).

35. Gupta, H., Deogharia, R., Sil, S., Singh, V. & Ray, A. On the interconnection of marine heatwaves and the extremely severe cyclonic storms Mocha and Biparjoy in the Northern Indian Ocean. *Natural Hazards* **121**, 18205-18225, doi:10.1007/s11069-025-07513-8 (2025).

36. Saranya, J. S., Roxy, M. K., Dasgupta, P. & Anand, A. Genesis and Trends in Marine Heatwaves Over the Tropical Indian Ocean and Their Interaction With the Indian Summer Monsoon. *Journal of Geophysical Research: Oceans* **127**, e2021JC017427, doi:https://doi.org/10.1029/2021JC017427 (2022).

37. Gupta, H., Sil, S., Gangopadhyay, A. & Gawarkiewicz, G. Observed surface and subsurface Marine Heat Waves in the Bay of Bengal from in-situ and high-resolution satellite data. *Climate Dynamics* **62**, 203-221, doi:10.1007/s00382-023-06913-5 (2024).

38. Kumar, S. *et al.* Analysis of marine heatwaves over the Bay of Bengal during 1982–2021. *Scientific Reports* **13**, 14235, doi:10.1038/s41598-023-39884-y (2023).

39. Wang, N. *et al.* A winter cold nights pattern in the Northern Hemisphere lands: Circum–hemisphere teleconnection of extreme cold events. *Climate Dynamics* **63**, 30, doi:10.1007/s00382-024-07486-7 (2024).

40. Tittensor, D. P. *et al.* Global patterns and predictors of marine biodiversity across taxa. *Nature* **466**, 1098-1101, doi:10.1038/nature09329 (2010).

41. Salas, S., Chuenpagdee, R., Seijo, J. C. & Charles, A. Challenges in the assessment and management of small-scale fisheries in Latin America and the Caribbean. *Fisheries Research* **87**, 5-16, doi:https://doi.org/10.1016/j.fishres.2007.06.015 (2007).

42. Zhang, Y., Du, Y., Feng, M. & Hu, S. Long-Lasting Marine Heatwaves Instigated by Ocean Planetary Waves in the Tropical Indian Ocean During 2015–2016 and 2019–2020. *Geophysical Research Letters* **48**, e2021GL095350, doi:https://doi.org/10.1029/2021GL095350 (2021).

43. Bader, J. & Latif, M. North Atlantic oscillation response to anomalous Indian Ocean SST in a coupled GCM. *JOURNAL OF CLIMATE* **18**, 5382-5389, doi:10.1175/JCLI3577.1 (2005).

44. Zhang, L. & Han, W. Indian Ocean Dipole leads to Atlantic Niño. *Nature Communications* **12**, 5952, doi:10.1038/s41467-021-26223-w (2021).

45. Latif, M., Dommenget, D., Dima, M. & Grötzner, A. The Role of Indian Ocean Sea Surface Temperature in Forcing East African Rainfall Anomalies during December–January 1997/98. *Journal of Climate* **12**, 3497-3504, doi:https://doi.org/10.1175/1520-0442(1999)012<3497:TROIOS>2.0.CO;2 (1999).

46. Ummenhofer, C. C., Sen Gupta, A., England, M. H. & Reason, C. J. C. Contributions of Indian Ocean Sea Surface Temperatures to Enhanced East African Rainfall. *Journal of Climate* **22**, 993-1013, doi:https://doi.org/10.1175/2008JCLI2493.1 (2009).

47. Zhao, S., Li, J. & Li, Y. Dynamics of an Interhemispheric Teleconnection across the Critical Latitude through a Southerly Duct during Boreal Winter. *Journal of Climate* **28**, 7437-7456, doi:https://doi.org/10.1175/JCLI-D-14-00425.1 (2015).

48. Li, Y. J., Li, J. P., Jin, F. F. & Zhao, S. Interhemispheric Propagation of Stationary Rossby Waves in a Horizontally Nonuniform Background Flow. *JOURNAL OF THE ATMOSPHERIC SCIENCES* **72**, 3233-3256, doi:10.1175/JAS-D-14-0239.1 (2015).

49. Li, Y., Feng, J., Li, J. & Hu, A. Equatorial Windows and Barriers for Stationary Rossby Wave Propagation. *Journal of Climate* **32**, 6117-6135, doi:https://doi.org/10.1175/JCLI-D-18-0722.1 (2019).

50. Li, J. *et al.* Influence of the NAO on Wintertime Surface Air Temperature over East Asia: Multidecadal Variability and Decadal Prediction. *Advances in Atmospheric Sciences* **39**, 625-642, doi:10.1007/s00376-021-1075-1 (2022).

51. Frankignoul, C. & Hasselmann, K. Stochastic climate models, Part II Application to sea-surface temperature anomalies and thermocline variability. *Tellus A: Dynamic Meteorology and Oceanography*, doi:10.3402/tellusa.v29i4.11362 (1977).

52. Thangaprakash, V. P. *et al.* What Controls Seasonal Evolution of Sea Surface Temperature in the Bay of Bengal? Mixed Layer Heat Budget Analysis Using Moored Buoy Observations Along 90°E. *Oceanography* **29** (2016).

53. Goswami, P., Gupta, H., Deogharia, R., Sil, S. & Pramanik, S. Contributions of upper layer processes on the mixed layer temperature in the Bay of Bengal using relative importance methods. *Ocean Dynamics* **74**, 935-948, doi:10.1007/s10236-024-01641-8 (2024).

54. Frankignoul, C. Sea surface temperature anomalies, planetary waves, and air-sea feedback in the middle latitudes. *Reviews of Geophysics* **23**, 357-390, doi:https://doi.org/10.1029/RG023i004p00357 (1985).

55. Frankignoul, C. in *Elsevier Oceanography Series* Vol. 25 (ed Jacques C. J. Nihoul) 35-55 (Elsevier, 1979).

56. Park, S., Deser, C. & Alexander, M. A. Estimation of the Surface Heat Flux Response to Sea Surface Temperature Anomalies over the Global Oceans. *Journal of Climate* **18**, 4582-4599, doi:https://doi.org/10.1175/JCLI3521.1 (2005).

57. Frankignoul, C., Czaja, A. & L'Heveder, B. Air–Sea Feedback in the North Atlantic and Surface Boundary Conditions for Ocean Models. *Journal of Climate* **11**, 2310-2324, doi:https://doi.org/10.1175/1520-0442(1998)011<2310:ASFITN>2.0.CO;2 (1998).

58. Hausmann, U., Czaja, A. & Marshall, J. Mechanisms controlling the SST air-sea heat flux feedback and its dependence on spatial scale. *Climate Dynamics* **48**, 1297-1307, doi:10.1007/s00382-016-3142-3 (2017).

59. Huang, J. & Bou-Zeid, E. Turbulence and Vertical Fluxes in the Stable Atmospheric Boundary Layer. Part I: A Large-Eddy Simulation Study. *Journal of the Atmospheric Sciences* **70**, 1513-1527, doi:https://doi.org/10.1175/JAS-D-12-0167.1 (2013).

60. Cabrera, M. *et al.* The southwestern Atlantic Ocean mesoscale eddies: A review of their role in the air-sea interaction processes. *Journal of Marine Systems* **235**, 103785, doi:https://doi.org/10.1016/j.jmarsys.2022.103785 (2022).

61. Chelton, D. & Xie, S. p. Coupled ocean-atmosphere interaction at oceanic mesoscales. *Oceanography* **23**, 52-69 (2010).

62. Small, R. J. *et al.* Air–sea interaction over ocean fronts and eddies. *Dynamics of Atmospheres and Oceans* **45**, 274-319, doi:https://doi.org/10.1016/j.dynatmoce.2008.01.001 (2008).

63. Chelton, D. B., Schlax, M. G., Freilich, M. H. & Milliff, R. F. Satellite Measurements Reveal Persistent Small-Scale Features in Ocean Winds. *Science* **303**, 978-983, doi:doi:10.1126/science.1091901 (2004).

64. Tokinaga, H., Tanimoto, Y. & Xie, S.-P. SST-Induced Surface Wind Variations over the Brazil–Malvinas Confluence: Satellite and In Situ Observations. *Journal of Climate* **18**, 3470-3482, doi:https://doi.org/10.1175/JCLI3485.1 (2005).

65. Wang, C. Three-ocean interactions and climate variability: a review and perspective. *Climate Dynamics* **53**, 5119-5136, doi:10.1007/s00382-019-04930-x (2019).

66. Kajtar, J. B., Santoso, A., England, M. H. & Cai, W. Tropical climate variability: interactions across the Pacific, Indian, and Atlantic Oceans. *Climate Dynamics* **48**, 2173-2190, doi:10.1007/s00382-016-3199-z (2017).

67. Wang, C. Z. Three-ocean interactions and climate variability: a review and perspective. *CLIMATE DYNAMICS* **53**, 5119-5136, doi:10.1007/s00382-019-04930-x (2019).

68. Kucharski, F. *et al.* The Teleconnection of the Tropical Atlantic to Indo-Pacific Sea Surface Temperatures on Inter-Annual to Centennial Time Scales: A Review of Recent Findings. *Atmosphere* **7**, 29 (2016).

69. Wang, C., Kucharski, F., Barimalala, R. & Bracco, A. Teleconnections of the Tropical Atlantic to the Tropical Indian and Pacific Oceans: A Review of Recent Findings. *Meteorologische Zeitschrift* **18**, 445-454, doi:10.1127/0941-2948/2009/0394 (2009).

70. Sen Gupta, A. *et al.* Drivers and impacts of the most extreme marine heatwave events. *Scientific Reports* **10**, 19359, doi:10.1038/s41598-020-75445-3 (2020).

71. Hu, S., Zhang, L. & Qian, S. Marine Heatwaves in the Arctic Region: Variation in Different Ice Covers. *Geophysical Research Letters* **47**, e2020GL089329, doi:https://doi.org/10.1029/2020GL089329 (2020).

72. Huang, B. Y. *et al.* Improvements of the Daily Optimum Interpolation Sea Surface Temperature (DOISST) Version 2.1. *JOURNAL OF CLIMATE* **34**, 2923-2939, doi:10.1175/JCLI-D-20-0166.1 (2021).

73. Kalnay, E. *et al.* The NCEP/NCAR 40-year reanalysis project. *BULLETIN OF THE AMERICAN METEOROLOGICAL SOCIETY* **77**, 437-471, doi:10.1175/1520-0477(1996)077<0437:TNYRP>2.0.CO;2 (1996).

74. Rustemeier Elke; Hänsel, S. F., Peter; Schneider, Udo; Ziese, Markus. GPCC Climatology Version 2022 at 1.0°: Monthly Land-Surface Precipitation Climatology for Every Month and the Total Year from Rain-Gauges built on GTS-based and Historical Data., doi:DOI: 10.5676/DWD_GPCC/CLIM_M_V2022_100 (2022).

75. Xie, P. & Arkin, P. A. Global Precipitation: A 17-Year Monthly Analysis Based on Gauge Observations, Satellite Estimates, and Numerical Model Outputs. *Bulletin of the American Meteorological Society* **78**, 2539-2558, doi:https://doi.org/10.1175/1520-0477(1997)078<2539:GPAYMA>2.0.CO;2 (1997).

76. Hersbach, H. *et al.* The ERA5 global reanalysis. *QUARTERLY JOURNAL OF THE ROYAL METEOROLOGICAL SOCIETY* **146**, 1999-2049, doi:10.1002/qj.3803 (2020).

77. Li, Y. J. & Li, J. P. Propagation of planetary waves in the horizontal non-uniform basic flow. *CHINESE JOURNAL OF GEOPHYSICS-CHINESE EDITION* **55**, 361-371, doi:10.6038/j.issn.0001-5733.2012.02.001 (2012).

78. Zhao, S., Li, J. P. & Li, Y. J. Dynamics of an Interhemispheric Teleconnection across the Critical Latitude through a Southerly Duct during Boreal Winter. *JOURNAL OF CLIMATE* **28**, 7437-7456, doi:10.1175/JCLI-D-14-00425.1 (2015).

79. Zhao, S., Li, J. P., Li, Y. J., Jin, F. F. & Zheng, J. Y. Interhemispheric influence of Indo-Pacific convection oscillation on Southern Hemisphere rainfall through southward propagation of Rossby waves. *CLIMATE DYNAMICS* **52**, 3203-3221, doi:10.1007/s00382-018-4324-y (2019).

80. Sardeshmukh, P. D. & Hoskins, B. J. The Generation of Global Rotational Flow by Steady Idealized Tropical Divergence. *Journal of Atmospheric Sciences* **45**, 1228-1251, doi:https://doi.org/10.1175/1520-0469(1988)045<1228:TGOGRF>2.0.CO;2 (1988).

81. Hoskins, B. J. & Karoly, D. J. The Steady Linear Response of a Spherical Atmosphere to Thermal and Orographic Forcing. *Journal of Atmospheric Sciences* **38**, 1179-1196, doi:https://doi.org/10.1175/1520-0469(1981)038<1179:TSLROA>2.0.CO;2 (1981).

82. Yang, Y. & Li, J. Novel monsoon indices based on vector projection and directed angle for measuring the East Asian summer monsoon. *Climate Dynamics* **63**, 210, doi:10.1007/s00382-025-07696-7 (2025).

83. Blackman, R. B. & Tukey, J. W. The Measurement of Power Spectra from the Point of View of Communications Engineering — Part I. *Bell System Technical Journal* **37**, 185-282, doi:https://doi.org/10.1002/j.1538-7305.1958.tb03874.x (1958).

84. Jenkins, G. M. & Watts, D. G. *Spectral analysis and its applications / Gwilym M. Jenkins and Donald G. Watts*. (Holden-Day, 1968).

85. Li, Y., Li, J. P. & Feng, J. A Teleconnection between the Reduction of Rainfall in Southwest Western Australia and North China. *JOURNAL OF CLIMATE* **25**, 8444-8461, doi:10.1175/JCLI-D-11-00613.1 (2012).

Acknowledgements

The authors would like to thank Yazhou Zhang, Yina Diao, Yang Zhao, Mian Zhu, and Hongqiang Dong for their help. We also thank the three anonymous reviewers for their constructive comments and suggestions, which greatly improved this manuscript.

Funding

J.L. and Z.L. acknowledge support for the research of this work from the National Natural Science Foundation of China (NSFC) Project (42288101), Laoshan Laboratory (No. LSKJ202202600), and Shandong Natural Science Foundation Project (ZR2019ZD12).

Author Contribution Statement

Z.L. conducted data analysis and model simulation, interpreted the results, generated the figures and wrote the original drafts. J.L. conceptualized the study, offered guidance in the research and manuscript development, and reviewed the final content.

Competing interests

The authors declare no competing interests

Figure Captions

Figure1. Correlation characteristics of Indian Ocean (IO) and Caribbean Sea (CS) marine heatwave indices (MHWI). a Lead-lag correlation map between the IO MHWI and CS MHWI for each month. The vertical axis represents the IO MHWI for each month, while positive (negative) values on the horizontal axis indicate the length of time (in months) by which the IO MHWI leads (lags) the CS MHWI. Green dashed line denotes regions exceeding the 95% confidence level. **b** The coherence spectrum (black) and lag spectrum (blue, unit: month) between the seasonal the previous-winter (December–February, DJF) IO MHWI and the following-spring (March–May, MAM) CS MHWI. Positive (negative) values on the blue vertical axis indicate the length of time (in months) by which the IO MHWI leads (lags) the CS MHWI. The horizontal axis shows the signal period (in years). Bold black lines denote above the 95% confidence level. **c** as in **b**, but for

seasonal DJF IO MHWI and the following-summer (June–August, JJA) CS MHWI. **d** Averaged IO MHWI (purple bars) and CS MHWI (blue bars) before and after intense IO MHW events. The dark-colored bars represent the portions with significance exceeding 95%. **e** Lead-lag correlation between the boreal winter (DJF) IO MHWI and CS MHWI. Bold lines denote above the 95% confidence level. horizontal axis indicate the center month of 3-month averaged CS MHWI.

Figure 2. The atmospheric circulation conditions during intense boreal winter (DJF) Indian Ocean (IO) marine heatwaves (MHWs). a Stationary Rossby wave trajectories at 200 hPa (green curves, zonal wavenumbers 1–7) computed in a horizontally non-uniform background flow. Starting points of wave rays (marked by cross) above the tropical Indian Ocean (30°–70°E, 0°–10°S). Shading shows the 200 hPa zonal wind field; contours indicate the meridional wind field (interval: 2 m s^{-1}, solid positive, dashed negative). Yellow contours outline regions of significant Rossby wave source (RWS) anomalies. Blue and red boxes indicate the definition regions of IO (50°–70°E, 0°–10°S) and Caribbean Sea (CS; 50°–85°W, 8°–24°N) MHW index, respectively. **b** 200 hPa meridional wind anomalies (shading) and horizontal Rossby wave ray flux (WRF; purple vectors, zonal wavenumbers 1–7) during intense DJF IO MHWs. Dots indicate the areas of stream function anomalies with the 95% confidence level. **c** as in **b** and green lines as in **a**, but for CAM6 simulation results.

Figure 3. Air–sea interaction of the Indo-Pacific-Atlantic Rossby wave train (IPAT) in the Caribbean Sea (CS) during intense boreal winter (DJF) Indian Ocean (IO) marine heatwaves (MHWs). a Distribution of 200 hPa divergence (isopleths, interval 10^6 s^{-1}) and 500 hPa Omega (shading) during intense DJF IO MHW. Dots indicate the areas with the 95% confidence level. Red boxes indicate the definition regions of CS MHWI (50°–85°W, 8°–24°N). **b** The latitude-height distribution of zonally averaged (50°–85°W) velocity anomalies (quivers), potential temperature (shading) and geopotential height (hgt, unit: gpm) anomalies (isopleths, interval 10 gpm) over Atlantic during intense DJF IO MHWs. The reference quiver (red, in white box) represents a horizontal wind speed of 1 m/s and a vertical velocity of 0.01 Pa/s. Note that the vertical velocity component is scaled by a factor of 100 for visualization. Black quivers (green dashed line) indicate velocity (geopotential height) confidence exceed 95% and solid (dashed) lines indicate positive (negative) values. **c** Surface latent heat flux anomalies (shading) and 925

hPa wind anomalies (quivers) in the North Atlantic Ocean region during intense DJF IO MHWs. Black quivers (dots) indicate velocity (flux) confidence exceed 95%. **d** Composite evolution of normalized anomalies of several variables averaged over the CS region following intense DJF IO MHWs: Hadley Cell Index (HCI; defined as the difference in zonal wind between 850 and 200 hPa), air–sea temperature difference (dT, positive indicates air is warmer), near-surface specific humidity (average of 1000 and 925 hPa), and surface latent heat flux (LH; positive downward).

Figure 4. Schematic of the mechanism linking boreal winter (DJF) Indian Ocean (IO) marine heatwaves (MHWs) to spring–summer (MAM–JJA) Caribbean Sea (CS) MHWs. a The IO MHWs in previous winter (DJF) accompanying the rise of the atmosphere. Then IO MHWs trigger a Rossby wave train propagating through the atmospheric bridge on the upper level, led to divergence anomaly on the upper level over the North Atlantic as well as the atmospheric thickness increase. **b** Abnormal Hadley circulation at the bottom layer led to the influx of moisture and temperature, as well as a decrease in wind speed, ultimately resulting in weakened evaporation, reduced latent heat loss, heating surface seawater, causing the CS MHWs activating concurrently. **c** Marine atmospheric boundary layer (MABL) is more stable and thinner with weakened vertical mixing, suppressing heat loss from the sea to the atmosphere and maintaining MHW activity from winter to spring (MAM) and summer over the CS.

Editorial summary: Winter marine heatwaves in the Indian Ocean can intensify spring and summer marine heatwaves in the Caribbean Sea through an atmospheric bridge. An eastward propagating wave train alters the regional Hadley circulation, reducing latent heat loss from the ocean and driving sea surface warming.

Peer Review Information: *Nature Communications* thanks Ségolène Berthou, Sourav Sil, and the other, anonymous, reviewer for their contribution to the peer review of this work. A peer review file is available.

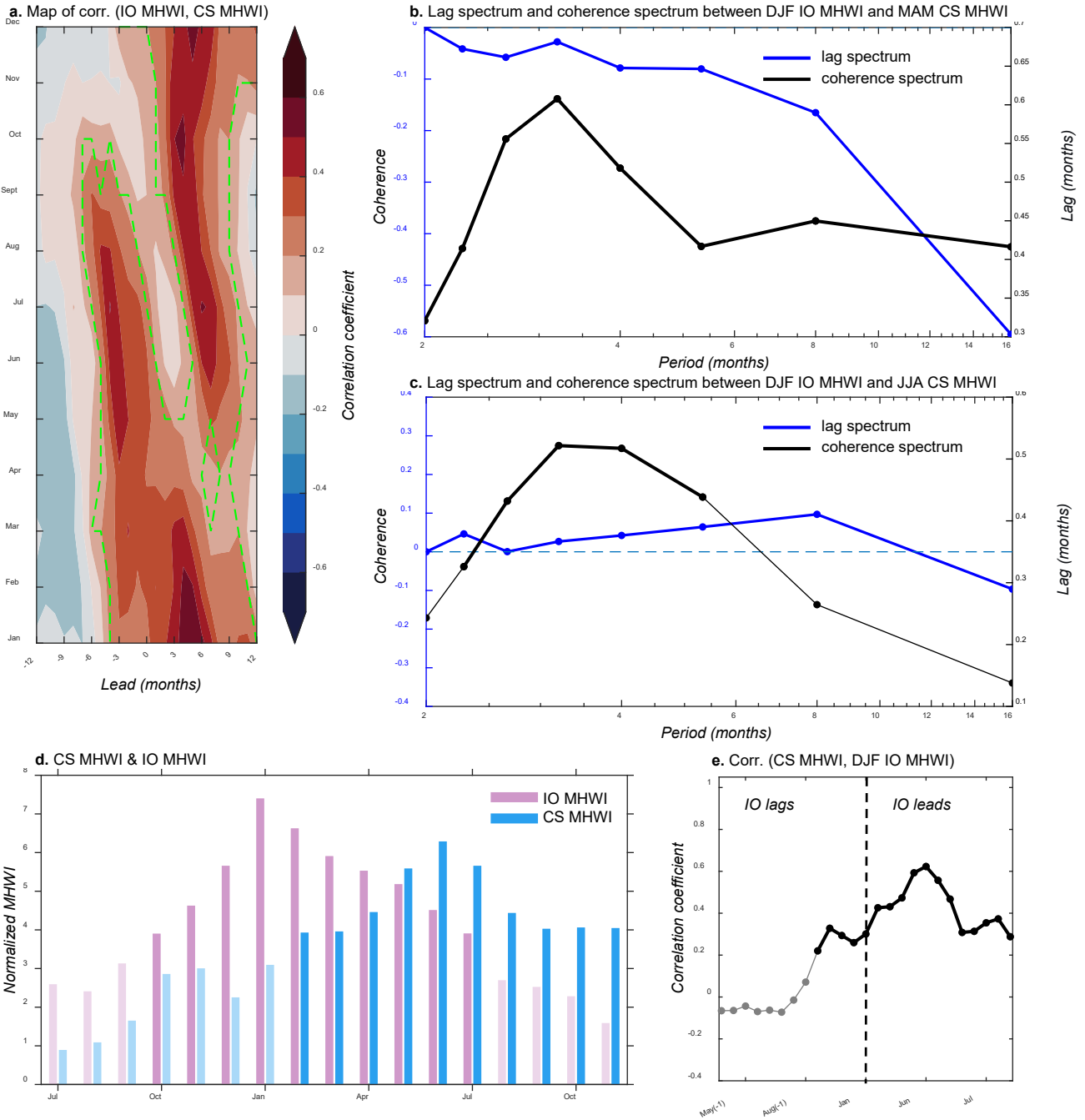
a. Map of corr. (IO MHWI, CS MHWI)
Dec
Nov
Oct
Sept
Aug
Jul
Jun
May
Apr
Mar
Feb
Jan
Lead (months)
Correlation coefficient
b. Lag spectrum and coherence spectrum between DJF IO MHWI and MAM CS MHWI
lag spectrum
coherence spectrum
Coherence
Lag (months)
Period (months)
c. Lag spectrum and coherence spectrum between DJF IO MHWI and JJA CS MHWI
lag spectrum
coherence spectrum
Coherence
Lag (months)
Period (months)
d. CS MHWI & IO MHWI
IO MHWI
CS MHWI
Normalized MHWI
Jul
Oct
Jan
Apr
Jul
Oct
e. Corr. (CS MHWI, DJF IO MHWI)
IO lags
IO leads
Correlation coefficient
May(-1)
Aug(-1)
Jan
Jun
Jul

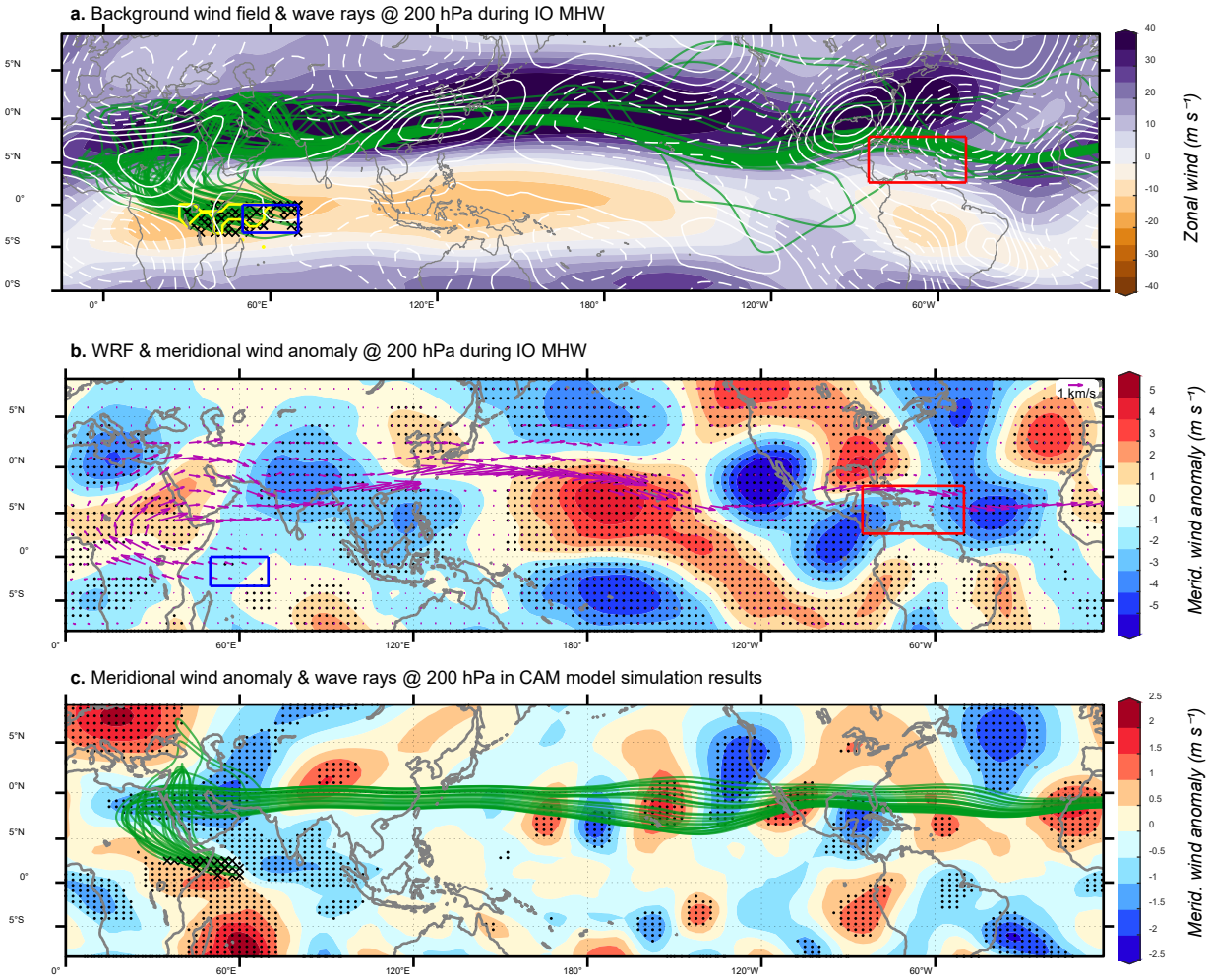
a. Background wind field & wave rays @ 200 hPa during IO MHW
Zonal wind (m s⁻¹)
b. WRF & meridional wind anomaly @ 200 hPa during IO MHW
1 km/s
Merid. wind anomaly (m s⁻¹)
c. Meridional wind anomaly & wave rays @ 200 hPa in CAM model simulation results
Merid. wind anomaly (m s⁻¹)
5°N
0°N
5°N
0°
5°S
0°S
0°
60°E
120°E
180°
120°W
60°W

a. Div. @ 200 hPa & omega @ 500 hPa during DJF IO MHW

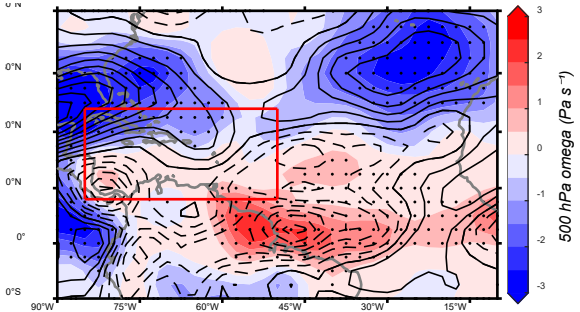

b. Zonal mean Hadley Celling & potential Temp. & hgt during DJF IO MHW

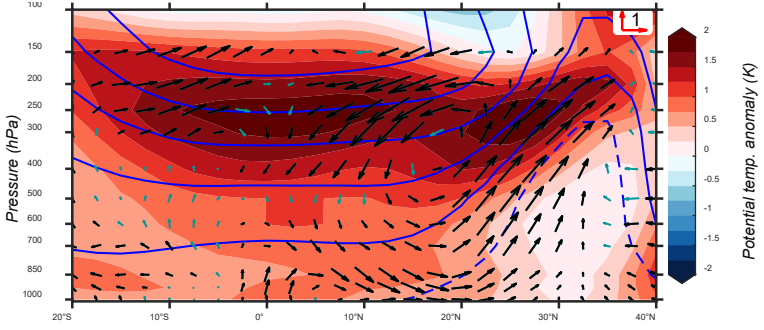

c. Low level wind & latent heat flux during DJF IO MHW

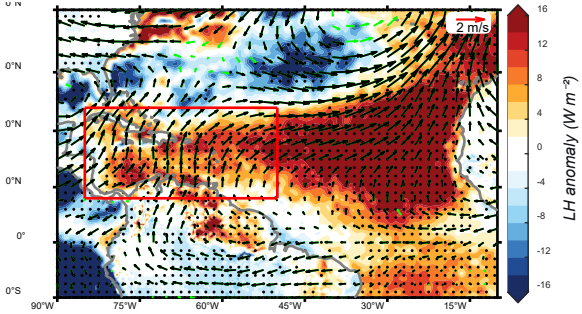

d. Composite analysis results of regional mean values before and after DJF IO MHW

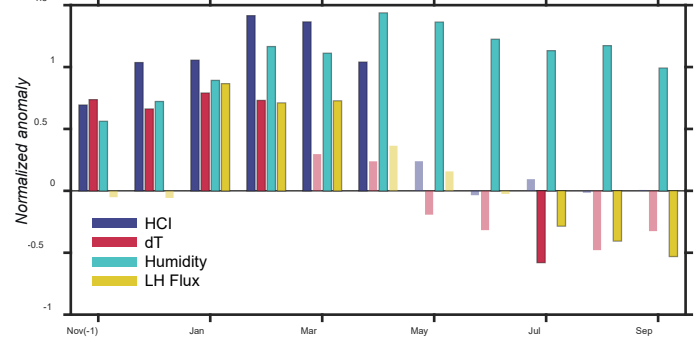

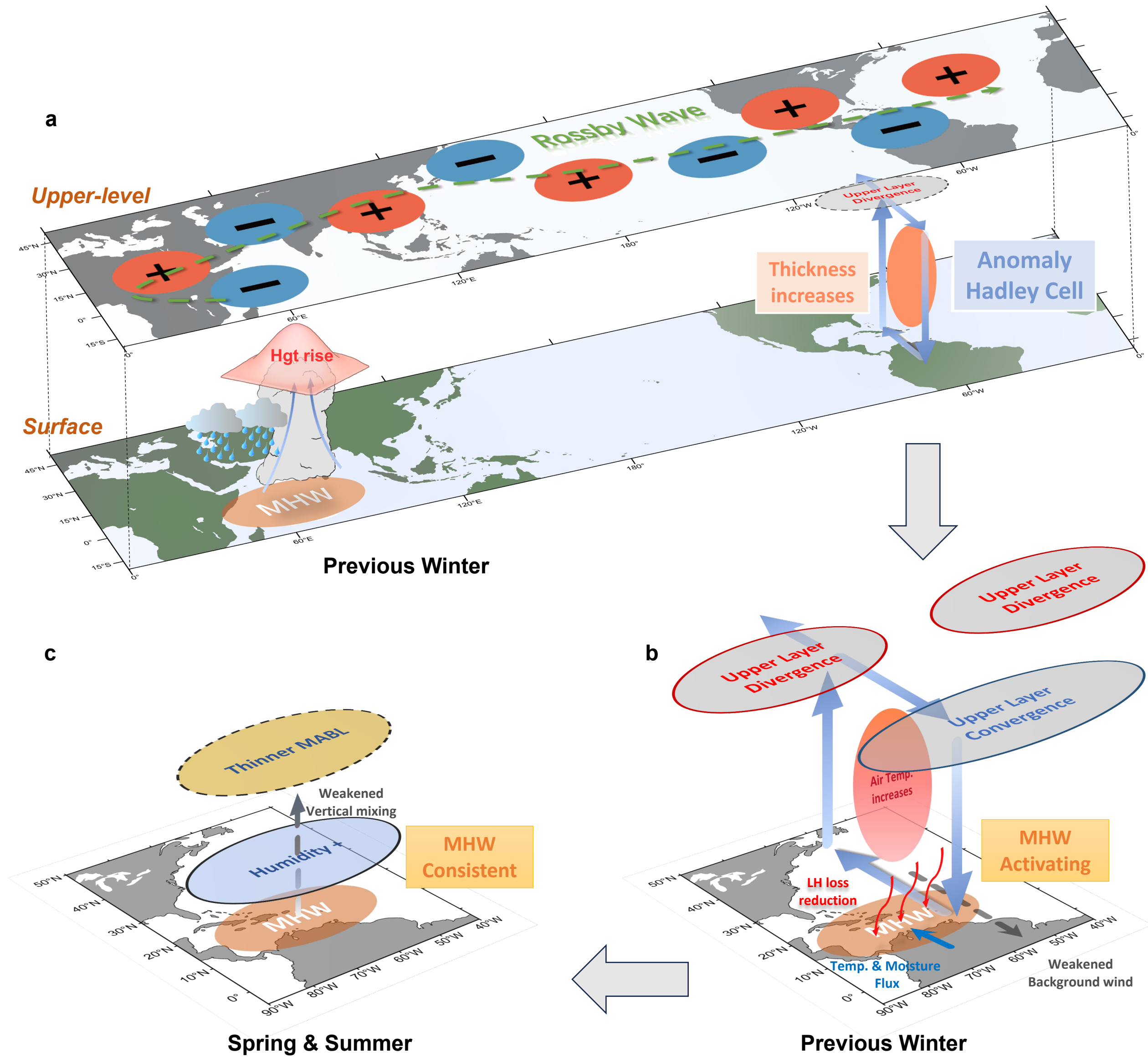
a
Upper-level
Rossby Wave
Upper Layer Divergence
Thickness increases
Anomaly Hadley Cell
Surface
Hgt rise
MHW
Previous Winter
Upper Layer Divergence
b
Upper Layer Divergence
Upper Layer Convergence
Air Temp. increases
LH loss reduction
MHW
MHW Activating
Temp. & Moisture Flux
Weakened Background wind
Previous Winter
c
Thinner MABL
Weakened Vertical mixing
Humidity +
MHW
MHW Consistent
Spring & Summer